Journal of Applied Physics

Acceptor levels of the carbon vacancy in *4H*-SiC: Combining Laplace deep level transient spectroscopy with density functional modeling

Cite as: J. Appl. Phys. **124**, 245701 (2018); https://doi.org/10.1063/1.5063773
Submitted: 01 October 2018 . Accepted: 02 December 2018 . Published Online: 26 December 2018

Ivana Capan, Tomislav Brodar, José Coutinho, Takeshi Ohshima, Vladimir P. Markevich, and Anthony R. Peaker

Acceptor levels of the carbon vacancy in 4*H*-SiC: Combining Laplace deep level transient spectroscopy with density functional modeling

Ivana Capan,[1] Tomislav Brodar,[1] José Coutinho,[2,a)] Takeshi Ohshima,[3] Vladimir P. Markevich,[4] and Anthony R. Peaker[4]
[1]*Division of Materials Physics, Ruder Bošković Institute, Bijenička 54, 10 000 Zagreb, Croatia*
[2]*Department of Physics and I3N, University of Aveiro, Campus Santiago, 3810-193 Aveiro, Portugal*
[3]*Takasaki Advanced Radiation Research Institute, National Institutes for Quantum and Radiological Science and Technology, 1233 Watanuki, Takasaki, Gunma 370-1292, Japan*
[4]*School of Electrical and Electronic Engineering and Photon Science Institute, University of Manchester, Manchester M13 9PL, United Kingdom*

(Received 1 October 2018; accepted 2 December 2018; published online 26 December 2018)

We provide direct evidence that the broad $Z_{1/2}$ peak, commonly observed by conventional deep level transient spectroscopy in as-grown and at high concentrations in radiation damaged 4*H*-SiC, has two components, namely, Z_1 and Z_2, with activation energies for electron emissions of 0.59 and 0.67 eV, respectively. We assign these components to $Z_{1/2}^{=} \rightarrow Z_{1/2}^{-} + e^{-} \rightarrow Z_{1/2}^{0} + 2e^{-}$ transition sequences from negative-*U* ordered acceptor levels of carbon vacancy (V_C) defects at hexagonal/pseudo-cubic sites, respectively. By employing short filling pulses at lower temperatures, we were able to characterize the first acceptor level of V_C on both sub-lattice sites. Activation energies for electron emission of 0.48 and 0.41 eV were determined for $Z_1(-/0)$ and $Z_2(-/0)$ transitions, respectively. Based on trap filling kinetics and capture barrier calculations, we investigated the two-step transitions from neutral to doubly negatively charged Z_1 and Z_2. Positions of the first and second acceptor levels of V_C at both lattice sites, as well as (=/0) occupancy levels, were derived from the analysis of the emission and capture data. *Published by AIP Publishing.*
https://doi.org/10.1063/1.5063773

I. INTRODUCTION

Owing to many advantages over silicon, silicon carbide (SiC), in particular its 4*H* polytype, is becoming a mainstream material for the industry of high-power electronics.[1,2] Due to its wide bandgap, radiation hardness, high breakdown field, and melting point, SiC is also a promising semiconductor for the fabrication of nuclear radiation detectors working in harsh environments, including at high temperature and dense radiation fields.[3–5]

SiC-based diodes for radiation detection are highly sensitive to defects that introduce deep carrier traps,[3] especially to those with large capture cross sections for minority carriers which hold the actual impact signal. Point defects in SiC are mainly created during (i) semiconductor material growth, (ii) device processing by ion-implantation, or (iii) during operation under radiation conditions.[6] It is therefore crucial to understand the effects of accumulated radiation damage on the electrical properties of these devices between ground states. In this work, we investigate single and double capture/emission processes involving a major recombination center in 4*H*-SiC, namely, the $Z_{1/2}$ electron trap, by combining space-charge measurements and first-principles calculations. The $Z_{1/2}$ trap is a prominent defect in 4*H*-SiC irradiated, for instance, with electrons or neutrons[7,8] and can be observed by conventional deep level transient spectroscopy (DLTS) as a conspicuous peak around room temperature.[9,10] It is usually present in the as-grown material with concentrations in the range of 10^{12}–10^{13} cm^{-3}, and it is strongly anchored to the lattice being stable up to about 1400 °C.[11–13] Early DLTS experiments by Hemmingsson *et al.*[14,15] assigned $Z_{1/2}$ to the superposition of two nearly identical Z_1 and Z_2 negative-*U* defect transitions, each located on a different sub-lattice site. The negative-*U* ordering of levels implies that during the two-electron filling of the defect, the binding energy (trap depth) of the second electron is higher than that of the first one. Hence, during the reverse process, the thermal emission of the first electron immediately induces a second emission.

More recently, by connecting electron paramagnetic resonance (EPR) and photo-EPR data with the DLTS results, it was possible to ascribe $Z_{1/2}$ to transitions involving the carbon vacancy (V_C) in 4*H*-SiC on distinct sub-lattice sites.[16] Furthermore, since the metastable EPR-active state was found to be the negative charge state, it became clear that the main $Z_{1/2}$ peak had to be connected to a $Z_{1/2}^{=} \rightarrow Z_{1/2}^{-} + e^{-} \rightarrow Z_{1/2}^{0} + 2e^{-}$ emission sequence. This is commonly labeled as $Z_{1/2}(=/0)$, where the first emission is the rate-limiting step, corresponding to the measured thermal activation energy (ΔE_a). We also note that based on carrier concentration profiles obtained at several temperatures using implanted/annealed samples, $Z_{1/2}$ cannot be a donor.[17]

In Ref. 14, the reported activation energies for electron emission were $\Delta E_a = 0.72$ eV and 0.52 eV for $Z_1(=/-)$ and $Z_1(-/0)$, respectively, while $\Delta E_a = 0.76$ eV and 0.45 eV for $Z_2(=/-)$ and $Z_2(-/0)$. It should be noted that negative-*U* defects undergo strong atomic relaxations upon emission/capture of carriers and may show relatively high barriers

a)Electronic mail: jose.coutinho@ua.pt

between different configurations.[18,19] Hence, activation energies for carrier emission often differ significantly from the values of the thermodynamic energy levels.[20] The latter are obtained by subtracting a capture barrier ΔE_σ from ΔE_a. While it was not possible to measure the temperature-dependence of the cross sections (and respective barriers) for the first electron capture, the second capture showed barriers of $\Delta E_\sigma = 65$ meV and 80 meV for Z_1 and Z_2, placing the (=/–) levels at $E_c - 0.67$ eV and $E_c - 0.71$ eV, respectively.[14]

Due to resolution limitations,[20,21] separate emissions from $Z_1^=$ and $Z_2^=$ cannot be resolved by conventional DLTS. To surmount this difficulty, activation energies and capture cross sections for Z_1(=/–) and Z_2(=/–) were estimated by fitting the data to biexponential capacitance transients subject to a fixed ratio between the two components (taken from the amplitude ratio of the first acceptors).[14] Hence, the measurements of the first and second acceptors could not be carried out independently, adding uncertainty to the measured levels.

These issues were partially addressed by some of us by means of high-resolution Laplace deep level transient spectroscopy (L-DLTS),[22] which allowed the observation of independent emissions from $Z_1^=$ and $Z_2^=$.[23] This technique had been previously employed in the separation of an analogous set of deeper traps, labeled $EH_{6/7}$, and attributed to donor transitions involving the V_C defect in 4*H*-SiC.[24] Laplace-DLTS was also successful in the study of E_1/E_2 traps observed in 6*H*-SiC samples.[25] Like $Z_{1/2}$, E_1/E_2 shows up as a prominent band in conventional DLTS spectra of the as-grown and irradiated material and has been attributed to a carbon vacancy.[26] Notably, from the Laplace spectra, it was demonstrated that the E_1/E_2 peak had contributions from three traps, namely, E_1 which showed the highest emission rate, plus two close deeper traps, E_{2L} and E_{2H}, with relatively lower and higher emission frequencies, respectively. The three peaks were assigned to emissions from equivalent defects located on all three sub-lattice sites of the 6*H* polytype (h, k_1, and k_2).[25]

The assignment of $Z_{1/2}$ to the carbon vacancy in 4*H*-SiC has been widely examined by first-principles modeling. While it is consensual that V_C introduces two acceptor levels in the upper half of the gap,[27–32] a clear negative-*U* ordering of levels was obtained only when spurious"periodic-charge" effects were neglected and uncorrected defect energies were used.[27–30] The most recent calculations which employed hybrid density functionals, besides not suffering from the severe underestimation of the bandgap as displayed by previous local and semi-local calculations, considered periodic-charge corrected energies. From these calculations, a negative-*U* of about −0.03 eV was obtained for the vacancy at the *k*-site [hereafter referred to as $V_C(k)$], while for the *h*-site the *U*-value was marginally positive (+0.03 eV).[30–32]

The V_C defect displays several structures, depending on the charge state and sub-lattice site.[30,32] These are denoted as $V_C(k, X)$ or $V_C(h, X)$, where $X \in \{A, B, C, D\}$ is an atomic configuration among those shown in the upper part of Fig. 1. The view is along the main axial direction [0001]. The four white circles are Si atoms, three located at basal corners and one at the apex of a triangular pyramid. The missing carbon atom would be located below the Si atom at the apex. Thick lines represent reconstructed bonds formed between the Si radicals. Structure A is the fully symmetric vacancy and it is adopted by the double-plus charge state only. In the lower part of Fig. 1, we also depict a calculated configuration coordinate diagram adapted from Ref. 32. Electronic transitions (and respective energies) are indicated by the vertical separation between different minima of the potential curves. For the *k*-site, the lowest energy states are $V_C^=(k, D)$, $V_C^-(k, D)$, and $V_C^0(k, B)$, while for the *h*-site, the most stable structures are $V_C^=(k, D)$, $V_C^-(k, C)$, and $V_C^0(h, B)$.

The location of the levels from the hybrid density functional calculations of Ref. 32 is rather close to the $Z_{1/2}$ levels, i.e., $V_C(k)$ was predicted to have levels at $E(-/0) = E_c - 0.61$ eV and $E(=/-) = E_c - 0.64$ eV, while $V_C(h)$ had levels at $E(-/0) = E_c - 0.67$ eV and $E(=/-) = E_c - 0.64$ eV. These transitions correspond to energy differences between the most stable structures for each charge state (see Fig. 1). Although the error bar of these calculations is ∼0.1 eV, the prediction of a deeper (–/0) transition of $V_C(h)$ combined with the more negative *U*-value for $V_C(k)$ strongly suggests that Z_1 and Z_2 should be ascribed to $V_C(h)$ and $V_C(k)$, respectively.[23]

The goal of the present study is to experimentally resolve the electronic transitions of Fig. 1 by means of high-resolution L-DLTS. The capture/emission kinetics and mechanisms ultimately depend on the activation energies and capture cross sections. The latter are hard to estimate—their calculation involves finding the electron-phonon coupling matrix elements describing a multi-phonon emission process (see Ref. 33 and references therein). Their evaluation is outside the scope of the present work. However, in order to get some insight into the capture/emission mechanisms, we calculated approximate values for the capture barriers of several transitions in Fig. 1. The paper is organized in the

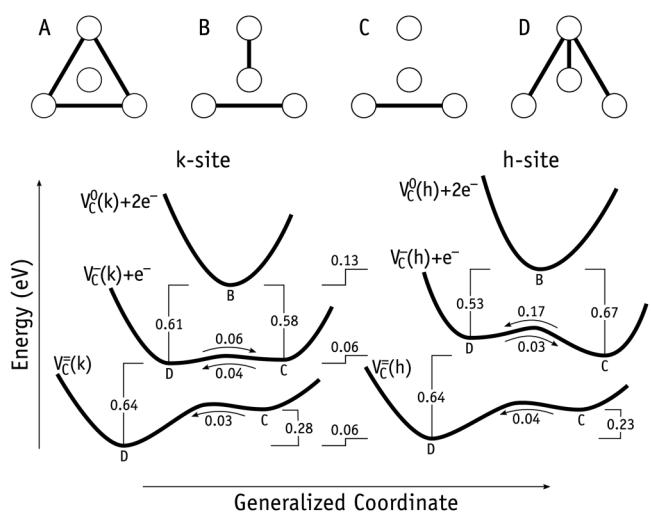

FIG. 1. (Top) structures of the carbon vacancy in 4*H*-SiC (charge state dependent). The [0001] axis is perpendicular to the plane of the figure. Outer circles forming a triangle are basal Si atoms, whereas the central circle represents an axial Si. Thick lines indicate the formation of reconstructed bonds between Si second neighbors. (Bottom) configuration coordinate diagram for the neutral, negative, and double negative V_C defect in 4*H*-SiC located on *k*- and *h*-sites. Transformation barriers are indicated next to the arrows. All energies in eV.

following way: In Sec. II, we describe the experimental and theoretical methodologies. Then in Sec. III, we report the conventional and Laplace DLTS data. In Sec. IV, we describe the calculated capture barriers. Finally, we discuss the results and draw conclusions in Sec. V.

II. EXPERIMENTAL AND THEORETICAL METHODS

Schottky barrier diodes (SBDs) were produced from epitaxially grown n-type 4*H*-SiC layers doped with nitrogen (up to 5×10^{14} cm^{-3}) with $\sim 25\,\mu$m thickness.[34] Schottky barriers were formed by evaporation of nickel through a metal mask with patterned square apertures of 1 mm $\times$1 mm, while Ohmic contacts were formed on the backside of the SiC substrate by nickel sintering at 950 °C in the Ar atmosphere.

The quality of the SBDs was investigated by current-voltage (*I-V*) and capacitance-voltage (*C-V*) measurements. A net doping concentration of 4.8×10^{14} cm^{-3} was obtained from the *C-V* measurements at 1 MHz and room temperature. Deep level defects were analyzed by means of DLTS and high-resolution L-DLTS to determine their respective activation energies for electron emission and capture cross sections. The DLTS measurements were performed in the temperature range 100–420 K at a ramp rate of 3 K/min, reverse bias $V_r = -10$ V, pulse bias $V_p = 0$ V, and pulse width $t_p = 1$ ms and using a rate window of 50 s^{-1}.

For the L-DLTS measurements,[22] capacitance transients were measured with the sampling rate, number of samples, and number of averaged scans in the range 5–80 kHz, 1200–9000, and 50–3000, respectively. Reverse and pulse biases were, respectively, $V_r = -5$ V and $V_p = 0$ V. Pulse widths were $t_p = 1$ ms and 100 ns for the (=/0) and (–/0) transitions, respectively. The estimated error of the temperature used in the L-DLTS measurements was less than 0.1 K.

For studying the capture kinetics, capacitance transients were measured with different pulse widths in the range 4×10^{-8}–5×10^{-4} s, while keeping the other parameters constant. In this case, reverse voltage and pulse voltage were, respectively, $V_r = -10$ V and $V_p = 0$ V. The sampling rate, number of samples, and number of averaged scans were in the range 4–80 kHz, 4000–8000, and 600–1500, respectively.

The Fermi level position at the temperature ranges where $Z_{1/2}$(=/0) and $Z_{1/2}$(–/0) emission peaks were observed was approximately 0.30 eV and 0.22 eV below E_c, respectively. So, in both cases, the Fermi level is significantly higher than the occupancy levels of the defects.

For the calculations, we employed the *Vienna Ab-initio Simulation Package* (VASP) code,[35–37] which implements a plane-wave based density functional method. Projector-augmented wave (PAW) potentials were used to describe the core electrons.[38] The PAW potentials for Si and C species were generated in the $3s^2 3p^2$ and $2s^2 2p^2$ valence configurations, respectively. We employed the generalized gradient approximation to the exchange-correlation energy as prescribed by Perdew *et al.*[39] The Kohn-Sham states were expanded in plane-waves with a cutoff energy of 420 eV.

Atomistic models of V_C defects were inserted in 400-atom 4*H*-SiC supercells, obtained by replication of $5 \times 5 \times 2$ unit cells (using the theoretical lattice parameters $a = 3.088$ Å and $c = 10.167$ Å). We employed a $2 \times 2 \times 1$ Monkhorst and Pack **k**-point grid to sample the Brillouin zone.[40] Structural optimization was carried out by means of a conjugate gradient method, with a convergence threshold of 5×10^{-3} eV/Å for the maximum force acting on the nuclei. The self-consistent electronic relaxation cycles were computed with an accuracy of 10^{-8} eV.

A. Classical capture barriers

Non-radiative capture of free carriers at deep traps often occurs via multi-phonon emission (MPE).[41–43] Within a classical harmonic picture, MPE capture can be described by means of a configuration coordinate diagram (CCD) as depicted in Fig. 2, which refers to the capture of electrons for the sake of convenience. It represents two parabolic potential energy curves, associated with free- ($|f^0 + e^-\rangle$) and trapped-electron ($|t^-\rangle$) states, with respective vibrational mode frequencies ω_f and ω_t, and energy minima separated by $\Delta Q = Q_f - Q_t$ in a generalized coordinate axis. In the energy axis, both states are separated by a transition level $\Delta E = E_c - E(-/0)$ below the conduction band bottom and they cross at ΔE_a.

MPE transitions take place close to the crossing-point of the two curves at a rate $c_n = \sigma_n \bar{v}_{n,th} n$,[44,45] which encodes the capture cross section of the trap (σ_n), the average thermal velocity of free electrons ($\bar{v}_{n,th}$), and their concentration (n). Broadly speaking, the capture cross section for a MPE transition is $\sigma_n = A_{ft}\Gamma$, where A_{ft} is a purely electronic term that describes the quantum mechanical tunneling rate between free and trapped electron states, while Γ is the often-called "line-shape function" describing the vibrational contribution to the transition rate.[41] These terms dominate σ_n at low and high temperatures, respectively. In the latter case, the capture process becomes thermally activated as $\sigma_n \sim \exp(-\Delta E_\sigma / k_B T)/\sqrt{T}$,[43] with k_B being the Boltzmann constant and ΔE_σ being a

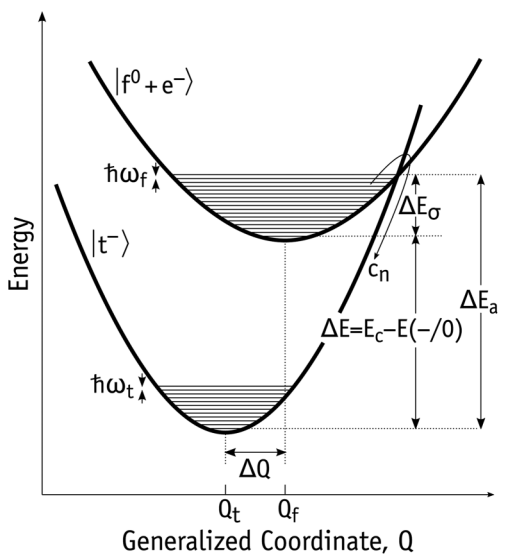

FIG. 2. Schematic configuration coordinate diagram describing the capture of an electron. Free-electron ($|f^0 + e^-\rangle$) and trapped-electron ($|t^-\rangle$) states are shown as parabolic curves. See text for a description of the quantities indicated.

capture barrier, i.e., the energy of the CCD crossing point with respect to the potential minimum of the free-electron state.

Obtaining σ_n from first-principles is an involved task (see, for instance, Refs. 46 and 33) which will not be attempted here. Alternatively, we will carry out a comparative analysis of the capture barriers for several transitions displayed in Fig. 1. To achieve this, we have to make bold assumptions. The first is that the vibronic system can be described by a single *effective* mode of vibration.[47,48] In such a one-dimensional CCD, the relevant parameters are the effective frequencies ω_f and ω_t, the modal mass M, and a modal vector connecting the atomic coordinates of N atoms of the free- and trapped-electron states, $\Delta\mathbf{R} = \mathbf{R}_f - \mathbf{R}_t = (\Delta\mathbf{r}_1, \ldots, \Delta\mathbf{r}_N)$. Here, $\Delta\mathbf{r}_\alpha = \mathbf{r}_{f;\alpha} - \mathbf{r}_{t;\alpha}$, with $\alpha = 1, \ldots, N$ and $\mathbf{r}_{\{f,t\};\alpha}$ being a Cartesian coordinate of the α-th atom.

The second assumption is that the harmonic approximation holds on both states. We define the generalized coordinate Q as[49]

$$Q^2 = \sum_\alpha m_\alpha \lambda^2 |\Delta\mathbf{r}_\alpha|^2, \tag{1}$$

which is obtained from linear interpolation of the coordinates weighted by atomic masses m_α, where λ is an arbitrary scalar. The units of Q are amu$^{1/2}$Å (amu—atomic mass unit). The modal mass

$$M = \frac{\sum_\alpha m_\alpha \Delta r_\alpha^2}{\sum_\alpha \Delta r_\alpha^2} \tag{2}$$

allows us to relate the atomistic distance ΔR with the separation in the CCD as $\Delta Q = M^{1/2}\Delta R$. Assuming that the origin of energy and coordinates is at the trapped state, the potential energy close to $\mathbf{R}_t$ is

$$E_t(Q) = \frac{1}{2}\omega_t^2 Q^2, \tag{3}$$

while near the free-carrier state, the potential energy is

$$E_f(Q) = \Delta E + \frac{1}{2}\omega_f^2 (Q - \Delta Q)^2, \tag{4}$$

where effective frequencies of vibration are obtained as $\omega_{\{t,f\}} = \partial^2 E_{\{t,f\}}/\partial Q^2$. Finally, the vibronic coupling can be quantified by the Huang-Rhys factor defined as

$$S_{\{t,f\}} = \frac{\omega_{\{t,f\}}(\Delta Q)^2}{2\hbar}, \tag{5}$$

which essentially quantifies the number of phonons emitted/created after optical (vertical) luminescence/absorption transitions. Cases where $S \approx 0$ and $S \gg 1$ correspond to weak and strong coupling and involve small and large defect relaxations, respectively.

Equations (3) and (4) were fitted to first-principles total energy data $E(q, \mathbf{R})$ obtained on a grid of coordinates $\mathbf{R} = \mathbf{R}_t + \lambda\mathbf{R}_f$, between fully relaxed structures in a specific charge state q. The calculated energy levels [ΔE in Eq. (4)] are those reported in Fig. 1. They were calculated using a hybrid density functional method,[32] which provides accurate energy differences between defects in different charge states. The present semi-local calculations of the harmonic potentials involve relative energies within the same charge state. The use of non-local functionals would not bring significant improvements.

III. EXPERIMENTAL RESULTS

Figure 3 shows a typical DLTS spectrum for the as-grown 4*H*-SiC material. The broad and asymmetric peak with a maximum at around 315 K with emission rate 50 s^{-1} is known as $Z_{1/2}$, and it was assigned to (=/0) transitions of V_C in 4*H*-SiC.[16] Like the E_1/E_2 peak in 6*H*-SiC, the asymmetry of the $Z_{1/2}$ peak of Fig. 3 hints a shoulder on the low-temperature side, suggesting the contribution of more than one defect, possibly differing on their sub-lattice sites. The blue solid line in Fig. 3 is the simulated DLTS spectrum (for the measurements conditions used) with contributions from two emission signals, the parameters of which have been determined from least-square fitting to the experimental data and are given in the graph. We suggest that the observed emission signals are related to the Z_1(=/0) and Z_2(=/−) transitions. Further arguments for such assignments are presented below. Concentrations of the Z_1 and Z_2 traps in the as-grown material studied are estimated to be about 9.5×10^{11} cm^{-3} and 2.1×10^{11} cm^{-3}, respectively.

Figure 4 shows high-resolution L-DLTS spectra measured on the same diode for which the conventional DLTS measurements are reported in Fig. 3. The values of the measurement temperature are in the range 325–330 K, i.e., near the temperature of the peak maximum of the $Z_{1/2}$ DLTS signal. The L-DLTS spectra of Fig. 4 clearly show that $Z_{1/2}$ consists of two close emission components. The results confirm those reported in Ref. 23, where the high- and low-frequency peaks, namely, Z_1(=/0) and Z_2(=/0), were

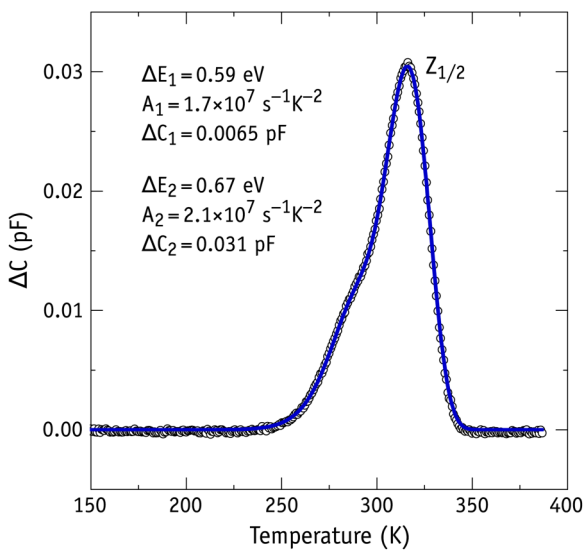

FIG. 3. Conventional DLTS spectrum (data points) obtained for an as-grown n-type 4*H*-SiC SBD. Reverse bias, pulse voltage, and width were $V_r = -10$ V, $V_p = 0$ V, and $t_p = 1$ ms, respectively. A rate window of 50 s^{-1} was used in the measurement. The blue solid line is the simulated DLTS spectrum with contributions from two emission signals, the parameters of which have been determined from a least-square fitting to the experimental data.

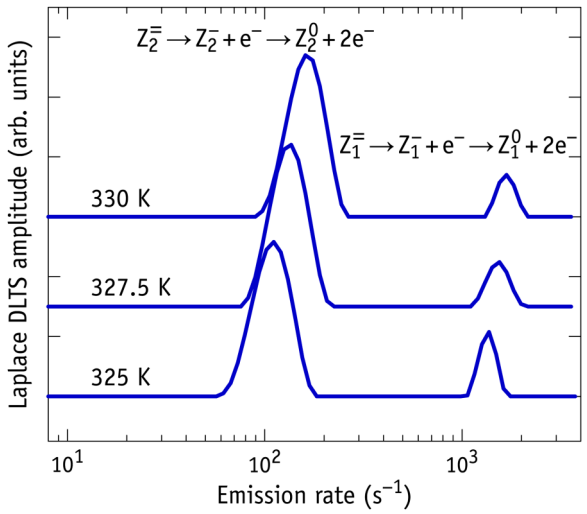

FIG. 4. L-DLTS spectra of the as-grown 4*H*-SiC SBD measured in the temperature range of the $Z_{1/2}$ peak maximum. Reverse bias, pulse voltage, and width were $V_r = -5$ V, $V_p = 0$ V, and $t_p = 1$ ms, respectively.

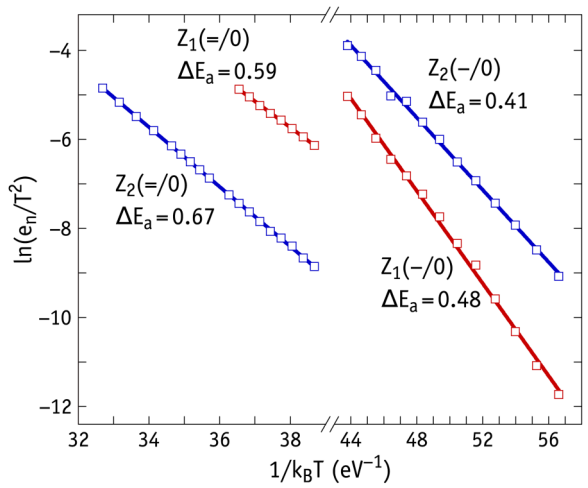

FIG. 5. Arrhenius plots of electron emission rates for $Z_1(=/0)$, $Z_2(=/0)$, $Z_1(-/0)$, and $Z_2(-/0)$ transitions in 4*H*-SiC obtained by L-DLTS measurements. Activation energies for electron emission are also shown for each peak. The horizontal axis is broken and separates double from single emissions. Pre-exponential factors and activation energies from the Arrhenius fits are reported in Table I.

ascribed to two-electron emission signals involving $V_C(h)$ and $V_C(k)$, respectively. Positions of the emission components do not change with varying acquisition settings (including numerical methods for the Laplace transform inversion), and, therefore, it is highly unlikely that the emission signals are related to numerical artifacts, which sometimes in the past were observed in L-DLTS spectra.[22]

Due to the negative-*U* ordering of the $Z_{1/2}$ levels, the emission of a second electron follows instantly after the emission of the first one. Hence, from the L-DLTS spectra, we only have access to activation energies for the first emission. Peak amplitudes shown in Fig. 4 are proportional to the change in capacitance of the space-charge and, therefore, account for both emissions. Hence, the observed two components of $Z_{1/2}$ relate to $Z_1^{=} \rightarrow Z_1^{-} + e^{-} \rightarrow Z_1^{0} + 2e^{-}$ and $Z_2^{=} \rightarrow Z_2^{-} + e^{-} \rightarrow Z_2^{0} + 2e^{-}$ sequential transitions. We note that the labeling of the second acceptors is consistent with that of the first acceptors in Ref. 14, where $Z_1(-/0)$ and $Z_2(-/0)$ were ascribed to the signals with lower and higher amplitudes, respectively.

From the L-DLTS peak intensities in Fig. 4, we estimate that the concentration ratio $[Z_2^{=}]:[Z_1^{=}]$ is 4.4 ± 0.2, suggesting that during growth Z_2 has a higher probability to form, most probably, because it is more stable. Previous conventional DLTS studies were not able to directly resolve these two components. The calculated formation energies of the vacancy on both sub-lattice sites indicate that $V_C(k)$ is more stable than $V_C(h)$,[32] supporting the assignment of Z_1 and Z_2 to $V_C(h)$ and $V_C(k)$, respectively.

From Arrhenius plots of T^2-corrected electron emission rates, activation energies for $Z_1(=/0)$ and $Z_2(=/0)$ transitions were determined as 0.59 eV and 0.67 eV, respectively. The Arrhenius fits to the data are shown in Fig. 5. The activation energies compare reasonably well with calculated second acceptor levels at $E_c - 0.64$ eV for both $V_C(h)$ and $V_C(k)$ defects. We should note that this comparison neglects any existing barrier for the capture of electrons. This issue will be addressed below.

For obtaining information about the shallower $Z_{1/2}(-/0)$ transitions and confirming the negative-*U* ordering of the acceptor levels, we have applied a procedure similar to that of Ref. 25, which enables one to freeze the negatively charged metastable configurations in the sample. Accordingly, we fully emptied the traps by cooling the diode from room temperature down to 220–270 K under reverse bias. The L-DLTS spectra were then recorded by applying a short (100 ns) filling pulse while keeping the number of scans below 50. Such conditions ensure that the number of injected electrons is far too low to double fill the traps and, therefore, emissions from double negative defects become small.

Figure 6 shows the L-DLTS spectra of as grown 4*H*-SiC SBD measured at various temperatures in the range 240–250 K. The measurements were carried out on the same SBD used to obtain the conventional DLTS spectrum shown in Fig. 3. In contrast to that spectrum and to the L-DLTS spectra recorded with the application of relatively long (ms range) filling pulses, the use of short pulses leads to the observation of two peaks in the L-DLTS spectra in the temperature range 220–250 K. The two emission signals are assigned to $Z_1(-/0)$ and $Z_2(-/0)$ transitions based on their relative magnitudes and emission rates. Interestingly, the $[Z_2^{-}]:[Z_1^{-}]$ magnitude ratio is 2.5 ± 0.7, differing from the

TABLE I. Activation energies (ΔE_a in eV), pre-exponential factors for the Arrhenius relation of the emission rate (A in $s^{-1}K^{-2}$), apparent capture cross sections (σ_a in cm^2), directly measured capture cross sections (σ_∞ in cm^2), and capture barriers (ΔE_σ in eV) for Z_1 and Z_2 defects in 4*H*-SiC as obtained by L-DLTS measurements.

Transition	ΔE_a	A	σ_a	σ_∞	ΔE_σ
$Z_1(=/0)$	0.59	1.1×10^7	2.7×10^{-15}	$> 10^{-15}$	~ 0
$Z_2(=/0)$	0.67	2.55×10^7	6.3×10^{-15}	2×10^{-16}	0.03
$Z_1(-/0)$	0.48	7.4×10^6	1.8×10^{-15}	$> 10^{-15}$	~ 0
$Z_2(-/0)$	0.41	2.15×10^6	5.25×10^{-16}	$> 10^{-15}$	~ 0

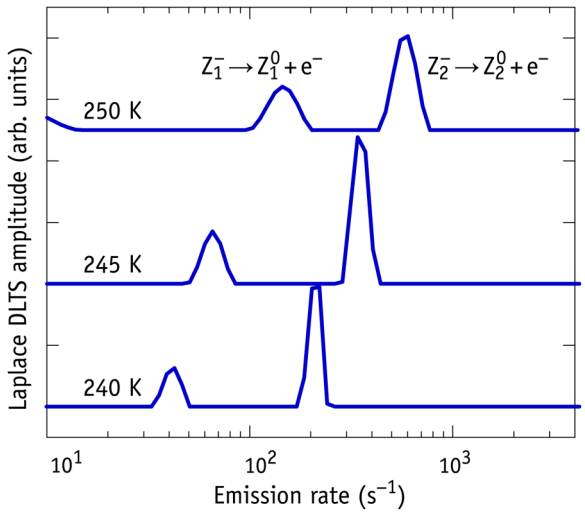

FIG. 6. L-DLTS spectra of as-grown 4*H*-SiC SBD measured at different temperatures in the range 240–250 K. Signals were obtained by applying short ($t_p = 100$ ns) filling pulses at low temperatures, allowing one to freeze the metastable negative states in the sample (see text for further details). Reverse and pulse voltages were $V_r = -5$ V and $V_p = 0$ V, respectively.

value obtained when longer filling pulses were applied and the traps were all double filled. We will return to this issue in Sec. V, where we will argue that this discrepancy could be due to kinetic effects during the filling pulse. Activation energies for electron emission were determined as 0.48 and 0.41 eV from Arrhenius plots of T^2-corrected emission rates of $Z_1(-/0)$ and $Z_2(-/0)$, respectively. These are shown on the right-hand side of Fig. 5.

We note that the magnitudes of the $Z_1(-/0)$ and $Z_2(-/0)$ peaks decrease as the number of filling pulses increases and eventually, disappear from the spectra after the application of a relatively large number of filling pulses. This indicates that an increasing fraction of double negatively charged $Z_{1/2}$ defects form and persist in the sample for the temperature range of the measurements. Such behavior is also a direct evidence for a negative-*U* ordering of the acceptor levels of $Z_{1/2}$—the repeated application of filling pulses results in the capture of a second electron by lingering $Z_{1/2}^-$ defects and, therefore, in the accumulation of $Z_{1/2}^=$ defects. The latter will stay in the double minus state, unless the temperature is raised up to room temperature.

As pointed out in Sec. I, negative-*U* defects show at least two atomic configurations, eventually separated by an energy barrier, and they may as well show considerable barriers for the capture of carriers. This means that activation energies for carrier emission, ΔE_a, may differ significantly from carrier binding energies, ΔE, which define the depth of the trap (or a transition level) with respect to the edge of the gap (see Fig. 2).[20] Capture barriers and carrier binding energies can be determined from combined emission and capture measurements as a function of temperature.

Besides measuring the activation energies for electron emission for all acceptor levels related to Z_1 and Z_2, we also carried out direct capture cross section measurements. We found that electron capture by neutral Z_1 and Z_2 traps is a very fast process. From measurements we could not observe significant changes in magnitudes of the $Z_1(-/0)$ and $Z_2(-/0)$ emission signals upon varying the length of the filling pulse in the range from 40 ns to 1 μs (in the temperature range 230–260 K). Considering the doping level of our samples, the position of the Fermi level and the shortest length of the filling pulse, we estimated a lower limit for the electron capture cross section of neutral Z_1 and Z_2 being 3×10^{-15} cm^2. These results suggest the existence of a minute or even vanishing capture barrier for both traps. So, it is likely that the depth of the first acceptor levels of Z_1 and Z_2 with respect to the conduction band bottom are essentially given by the activation energies for electron emission, i.e., they should be located at $E_c - 0.48$ eV and $E_c - 0.41$ eV, respectively.

Figure 7 shows how the magnitude of the $Z_1(=/0)$ and $Z_2(=/0)$ emission signals change with the length of the filling pulse. The data were obtained by L-DLTS at $T = 325$ K. For very short pulses(< 100 ns), the number of double filled $Z_{1/2}$ traps is negligible, while for pulses longer than 10 μs the signals saturate due to complete double filling. We found that the time-dependence of the signals (measured as capacitance transients of the diode, ΔC) was satisfactorily described by a mono-exponential law

$$\Delta C(t) = \Delta C_{max}[1 - \exp(-t/\tau)], \quad (6)$$

where ΔC_{max} is the maximum amplitude of the signal and τ is the characteristic time of the capture transient. $1/\tau$ is the defect occupancy rate, which for defects in the n-type material can be expressed as[44,45]

$$1/\tau = e_n + C_n n, \quad (7)$$

where e_n is the electron emission rate, C_n is the electron capture coefficient, and n is the concentration of free electrons in the conduction band. The first and the second terms are dominant in Eq. (7) when the Fermi level is below or above the defect occupancy level, respectively. The capture

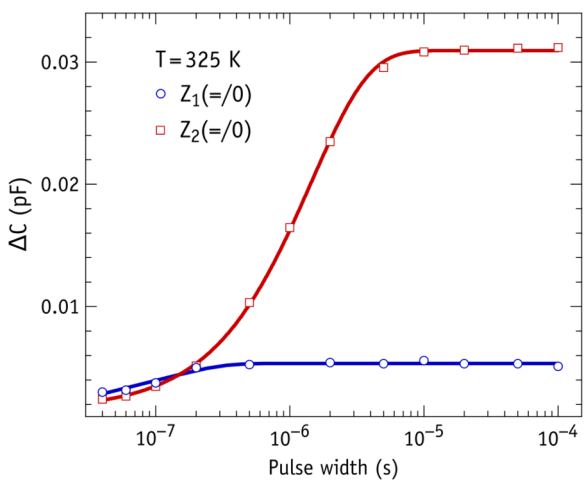

FIG. 7. Capture kinetics measured for $Z_1(=/0)$ and $Z_2(=/0)$ transitions by L-DLTS at $T = 325$ K. Data points are the magnitude of the L-DLTS peaks for different durations of the filling pulse. Solid lines represent best fits of the data to Eq. (6).

coefficient for defects with U > 0 is expressed as

$$C_n = \sigma_n \bar{v}_{n,th}, \tag{8}$$

where σ_n is the electron capture cross section and $\bar{v}_{n,th}$ is the average thermal velocity of free electrons. In general, the capture cross section is a temperature-dependent quantity. For the capture process occurring via multi-phonon emission, the capture cross section can be described by[43]

$$\sigma_n = \sigma_{n\infty} \exp(-\Delta E_\sigma / k_B T), \tag{9}$$

where ΔE_σ is the barrier for capture and $\sigma_{n\infty}$ is the capture cross section at infinitely high temperature.

The occupancy statistics for defects with negative-U properties was considered in Ref. 19. It was shown that Eq. (7) is also valid for the defects with $U < 0$, however, with more complicated equations for e_n and C_n. Emission of electrons by a negative-U defect with net-charge $q-2$ becomes a dominant process when the Fermi level lies below an occupancy level $E(q-2/q) = [E(q-1/q) + E(q-2/q-1)]/2$. For $E_F > E(q-2/q)$, capture is more effective than emission and, therefore,[19]

$$1/\tau = C_n^{eff} n.$$

It was found that in this case, up to four different terms can contribute to $1/\tau(T)$, depending on the position of Fermi level with respect to the $E(q-2/q-1)$ level and its configurations in the $q-1$ charge state.[19]

When analyzing the capture results presented in Fig. 7, we have taken into account the position of the Fermi level with respect to $Z_{1/2}(=/-)$ and $Z_{1/2}(-/0)$ defect levels and the configuration structure of V_C at k and h lattice sites in the singly negatively charged states (cf. Fig. 1). It has been concluded that in this case, $1/\tau(T)$ can be expressed as

$$1/\tau = \sigma_n \bar{v}_{n,th} n. \tag{10}$$

The solid curves in Fig. 7 represent the best fits of Eq. (6) to the $Z_{1/2}(=/0)$ capture transient data, from which we extracted values of ΔC_{max} and τ. Due to its weak magnitude, combined with the sensitivity limits of the equipment, we could not determine the characteristic time of the capture process for $Z_1(=/0)$. According to Eq. (7) a lower limit for the capture cross section of $Z_1(=/0)$ was estimated to be 10^{-15} cm^2, corresponding to a rather small capture barrier. Combining these findings with those above which indicate a vanishing capture barrier for $Z_1(-/0)$ as well, we conclude that the depth of the $Z_1(=/-)$ trap is essentially the activation energy for electron emission from the double negative charge state, i.e., the level should be at about $E_c - 0.59$ eV.

The capture kinetics for $Z_2(=/0)$ was measured in the temperature range 300–350 K. The Fermi level lies well above the metastable $Z_2(-/0)$ level which is estimated at 0.41 eV below the conduction band edge. This ensures that we avoid the formation of singly negative metastable states during the filling pulse. Considering the observed fast capture of electrons by neutral Z_2, the thermally activated capture kinetics of $Z_2(=/0)$ shown Fig. 7 must be limited by the capture of the second electron by singly negative Z_2^- defects. These observations also suggest that the geometry of

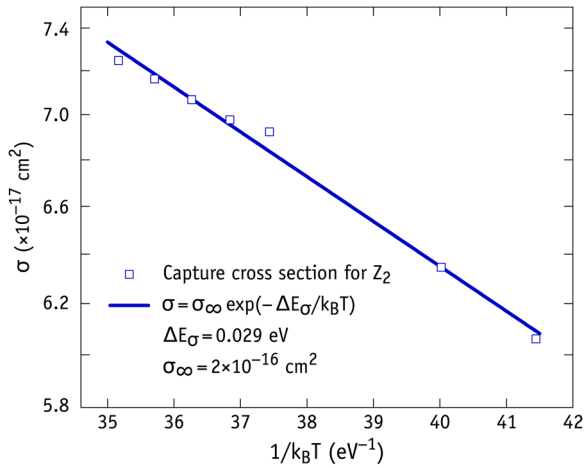

FIG. 8. Temperature dependence of the electron capture cross section of $Z_2(=/0)$. The solid line represents the best fit of the data to an Arrhenius relation describing a thermally activated capture process. The best values obtained for the capture barrier (ΔE_σ) and direct capture cross section (σ_∞) are also shown.

Z_1 and Z_2 defects should evolve differently along the capture sequence. The temperature dependence of the capture cross section as derived from the experimental data and the use of Eqs. (6) and (10) are presented in Fig. 8. The data can be satisfactorily described by Eq. (9), with $\sigma_\infty = 2 \times 10^{-16}$ cm^2 and $\Delta E_\sigma = 0.029 \pm 0.005$ eV. Combining the activation energy for electron emission from double negative Z_2 with the electron capture barrier of single negative Z_2, we arrive at a $Z_2(=/-)$ transition at $E_c - 0.64$ eV.

IV. CALCULATION OF CAPTURE BARRIERS

Now, we describe our calculations of the capture barriers for neutral and negatively charged carbon vacancies in 4*H*-SiC. Figure 1 shows that for neutral V_C, the capture process departs from $V_C^0(B) + e^-$ and can, in principle, arrive either at $V_C^-(C)$ or $V_C^-(D)$. For now, we are dropping the sub-lattice label (k and h) in the notation of the defect state as in this particular case, the picture is analogous for both pseudo-cubic and hexagonal vacancies. Hence, for each sub-lattice site, we have to consider two effective coupling modes, namely, Q_{C^-/B^0} and Q_{D^-/B^0}. These were calculated by combining Eq. (1) along with modal vectors $\Delta\mathbf{R} = \mathbf{R}_{B^0} - \mathbf{R}_{C^-}$ and $\Delta\mathbf{R} = \mathbf{R}_{B^0} - \mathbf{R}_{D^-}$. They connect the end-coordinates $\mathbf{R}_{X^q}$ of ground-state configurations X in charge state q (see Sec. II).

For electron capture by negatively charged vacancies, Fig. 1 shows that $V_C^-(C) + e^-$ and $V_C^-(D) + e^-$ have close relative energies, particularly for the k-site, and are separated by small barriers. We, therefore, considered C and D initial structures to estimate the capture barriers of vacancies at both k- and h-sites. Regarding the final state, clearly $V_C^=(D)$ is the most stable configuration on both sites, but since $V_C^=(C)$ can easily transform to $V_C^=(D)$, we also considered capture routes such as $V_C^-(C) + e^- \rightarrow V_C^=(C)$. Hence, for the second acceptor, and for both $V_C(k)$ and $V_C(h)$, we have direct-modes $Q_{C^=/C^-}$ and $Q_{D^=/D^-}$, as well as cross-modes $Q_{C^=/D^-}$ and $Q_{D^=/C^-}$.

The CCDs were produced by fitting Eqs. (3) and (4) to 11 data points within $|Q - Q_0| \leq 0.5$ amu$^{1/2}$Å around the

minimum energy coordinate Q_0 of each state. Figures 9(a) and 9(b) show calculated CCDs for several (=/–) transitions involving $V_C(k)$ and $V_C(h)$, respectively. Ground state and metastable configurations are represented in blue and red colors, respectively. Energy differences between different charge states, i.e., the electronic levels, were taken from Ref. 32 and are shown in Fig. 1. Besides the data points used for the fittings, additional points were calculated at $|Q - Q_0| > 0.5\ \text{amu}^{1/2}\text{Å}$ to provide us an idea of how much the potential energy deviates from the harmonic regime. The origin of coordinates and energy was assumed at the trapped state, $V_C^-(D)$.

From the fittings, effective mode frequencies in the range $\omega \sim 200 - 300\ \text{cm}^{-1}$ were obtained. These are consistent with vibrations involving weak Si-Si reconstructed bonds edging the vacancy defects. These frequencies should be compared to $520\ \text{cm}^{-1}$, which is the Raman frequency involving stiffer Si-Si bonds in bulk Si. According to Stoneham,[47] the relative positioning of the initial state (before capture) with respect to the final state (after capture) can be described by a coupling ratio

$$\Lambda = \frac{S}{S+p}, \tag{11}$$

where S is the Huang-Rhys factor, while $p = \Delta E/\hbar\omega$ is the number of phonons spanning the zero-phonon energy.

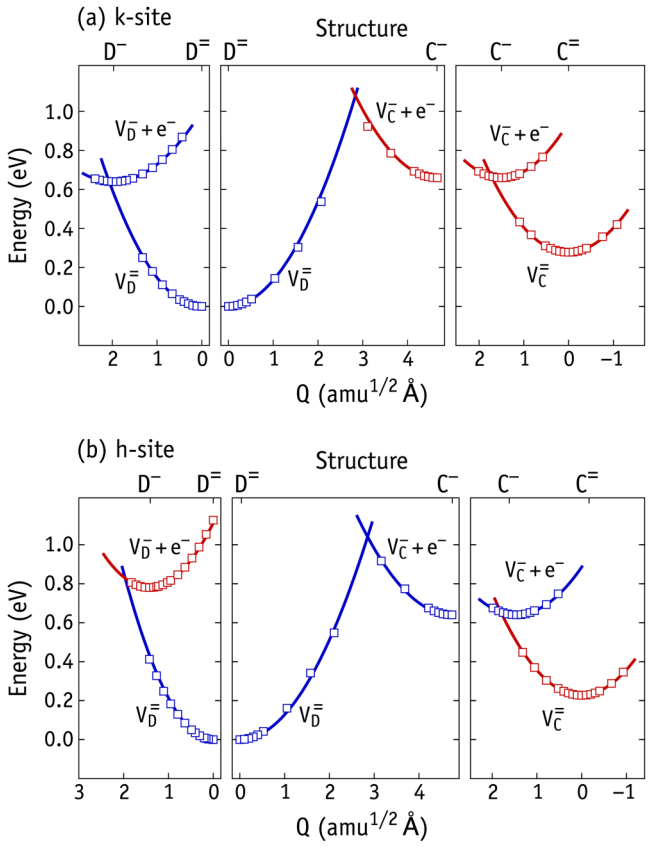

FIG. 9. Calculated configuration coordinate diagram of (a) pseudo-cubic and (b) hexagonal carbon vacancies in 4*H*-SiC, illustrating capture barriers for V_C^-. Ground state and metastable configurations are shown in blue and red, respectively. See text for a quantitative description of the configuration coordinate Q. The origin of the energy scale was set at the double minus ground state.

Accordingly, three distinctive situations may occur: (i) $\Lambda \to 0$ which represents the weak coupling limit, where $\Delta Q \sim 0$, i.e., the coordinates of both states involved are nearly coincident; (ii) $\Lambda = 1/2$ representing a strong coupling case where the potential energy curve of the final state (lower parabola) crosses the initial state (upper parabola) at its minimum energy; and (iii) $\Lambda \to 1$ implies that $S \to \infty$, representing the *absurd* limit where initial and final states become infinitely distant in the configurational space. We also note that for $\Lambda < 1/2$ and $\Lambda > 1/2$, the minimum of the upper parabola falls inside and outside the lower parabola, respectively. Examples of $\Lambda < 1/2$ and $\Lambda > 1/2$ arrangements are shown, respectively, on the left and middle insets of Fig. 9(a).

In broad terms, for the first capture ($V_C^0 + e^- \to V_C^-$), and irrespectively of the lattice site, we found that both Q_{C^-/B^0} and Q_{D^-/B^0} effective modes lead to $\Lambda \sim 0.5$ and, therefore, to rather small capture barriers $\Delta E_\sigma = 20{-}30$ meV. Their height is in line with the weak response of the $Z_{1/2}(-/0)$ L-DLTS peaks as a function of the pulse time. Taking into account the low transformation barriers that separate ground state structures $V_C^-(k, D)$ and $V_C^-(h, C)$ from metastable $V_C^-(k, C)$ and $V_C^-(h, D)$, respectively (see Fig. 1), the above results are unable to decide on any of the two possible capture routes under scrutiny.

For electron capture by the negatively charged V_C^- defects, transitions involving direct modes ($Q_{D^=/D^-}$ and $Q_{C^=/C^-}$) also show Λ values near 0.5. Consequently, these modes lead to capture barriers not higher than 50 meV. The calculated data and fitted parabolas are shown on the right and left insets of Figs. 9(a) and 9(b) for $V_C(k)$ and $V_C(h)$, respectively.

Unlike the above modal distances ($\Delta Q_{D^=/D^-} \sim \Delta Q_{C^=/C^-} \sim 2\ \text{amu}^{1/2}\text{Å}$) or those involved in the first acceptor ($\Delta Q_{C^-/B^0} \sim \Delta Q_{D^-/B^0} \sim 2\ \text{amu}^{1/2}\text{Å}$), configurations C and D are remote from each other in the configurational space ($\Delta Q_{C^=/D^-} \sim \Delta Q_{D^=/C^-} \gtrsim 5\ \text{amu}^{1/2}\text{Å}$). For that reason, transitions coupled to $Q_{C^=/D^-}$ and $Q_{D^=/C^-}$ cross modes show a large $\Lambda \gtrsim 0.8$ and large barriers are expected. For these transitions, we estimated capture barriers of at least 0.4 eV [see, for example, the middle insets of Figs. 9(a) and 9(b)].

V. DISCUSSION AND CONCLUSIONS

Before the concluding remarks, we provide a critical view on three pending issues:

Error bars related to the calculated capture barriers: The calculated capture barriers are in some cases of the order of tens of meV. Considering the many approximations involved, the error bars for calculated ΔE_σ values are probably of the order of 0.1 eV. While it is possible to conclude that most capture barriers are small (except those involving cross-modes), we will restrain ourselves from drawing quantitative conclusions based on the calculated barriers.

Calculated population ratios: It is known that above 1400 °C vacancies are able to migrate.[13] During the cooling of as-grown crystals, vacancies will *freeze* as the temperature drops below that threshold with a corresponding thermalized population ratio. At such temperatures the material is intrinsic so that V_C defects will essentially adopt the neutral charge

state. Taking into account the calculated energy difference between $V_C^0(k)$ and $V_C^0(h)$ of 0.13 eV [see Fig. 1], from the Boltzmann statistics, we obtain a $[Z_2]$:$[Z_1] \sim 2.5$, i.e., almost half of the experimental value reported in Sec. III from emissions by $Z_{1/2}^{=}$ defects. A 4.4 ratio would be obtained at 1400 °C only if $V_C^0(k)$ was more stable than $V_C^0(h)$ by 0.2 eV. Considering that (i) the population ratio in the sample may not even reflect thermodynamic equilibrium conditions, (ii) the error bar for the calculated formation energies is at least 0.1 eV, and (iii) configurational and vibrational entropy should be very similar for analogous defects at k and h sites, we must conclude that any quantitative account for the observed population ratio by the current theory level is highly speculative.

Different Z_1:Z_2 amplitude ratios for first and second acceptors: We must consider the possibility that the amplitude ratio $[Z_1^-]$:$[Z_2^-]$ for the first acceptor (Fig. 6) could reflect a flawed $[Z_1]$:$[Z_2]$ population ratio. First, we note that both neutral Z_1 and Z_2 have almost vanishing capture barriers. That leaves us with a capture kinetics dominated by the quantum mechanical tunneling probability at the transition state, which is embodied by the direct capture cross section. Table I shows that Z_1 traps have larger capture cross sections than Z_2. Hence, during a very short filling pulse, the formation of Z_1^- will be favored in the detriment of Z_2^-. This could result in a deceiving $[Z_2^-]$:$[Z_1^-] \sim 2.5$ ratio which underestimates the true $[Z_2]$:$[Z_1] \sim 4.4$ concentration ratio obtained from $Z_{1/2}(=/0)$ transitions (Fig. 4).

If Z_1^0 and Z_2^0 are in fact $V_C^0(h, B)$ and $V_C^0(k, B)$ defects which differ in their second neighboring ligands only, one wonders why do they show such different capture cross sections? A possible reason can be found not only in the vacancy states but also in the localization of the lower conduction band states of 4*H*-SiC. From inspection of the local density of states (LDOS) of bulk 4*H*-SiC close to the conduction band minima and from plots of $|\psi(\mathbf{r})|^2$, we found that the localization is mostly found on Si(k)-C(k) dimers and nearly vanishes on Si(h)-C(h) dimers. Since $V_C^0(h)$ is edged by three Si(k) atoms and one Si(h) radicals, we expect a larger overlap between the acceptor states of $V_C^0(h)$ and the conduction band minimum states. On the other hand, $V_C^0(k)$ has only one Si(k) and three Si(h) radicals, resulting in a defect with lower capture cross section than $V_C^0(h)$. These arguments not only support the above arguments regarding the capture kinetics but also support the assignment of Z_1 and Z_2 to the carbon vacancy at the h and k lattice sites.

Now, we compare the electronic properties of $Z_{1/2}$ with those of the carbon vacancy in 4*H*-SiC. We found that both Z_1 and Z_2 show a negative-U ordering for the acceptor levels. Z_2 has the larger correlation energy ($U = -0.23$ eV) with levels at $E(-/0) = E_c - 0.41$ eV and $E(-/0) = E_c - 0.64$ eV, while Z_1 has levels separated by only $U = -0.11$ eV and they are located at $E(-/0) = E_c - 0.48$ eV and $E(-/0) = E_c - 0.59$ eV, both lying right between $Z_2(-/0)$ and $Z_2(=/-)$. In fact, both $Z_1(=/0)$ and $Z_2(=/0)$ occupancy (thermodynamic) levels coincide at $E_c - 0.53$ eV, i.e., at mid-way between their respective metastable acceptors. These results agree well with the most recent calculations,[31,32] where (=/0) occupancy levels for $V_C(k)$ and $V_C(h)$ were estimated at $E_c - 0.63$ eV and $E_c - 0.65$ eV, but more significantly $V_C(k)$ showed a negative $U = -0.03$ eV, while $V_C(h)$ had a marginally positive $U = +0.03$ eV, supporting direct connections between $Z_{1/2}$ and $V_C(h/k)$, respectively.

Before discussing the mechanisms for electron capture, it is important to note that EPR confirms that negatively charged $V_C^-(k)$ and $V_C^-(h)$ defects show D and C ground state structures, respectively.[30,32] Alternative $V_C^-(k, C)$ and $V_C^-(h, D)$ configurations are metastable and can easily be converted to the ground states by surmounting energy barriers of the order of 0.1 eV and lower (see Fig. 1).

The measurements indicate that the capture barriers for $V_C^0 + e^- \rightarrow V_C^-$ are very small (or even vanishing). The calculated capture barriers were also found to be very small for transitions involving ground state modes Q_{D^-/B^0} and Q_{C^-/B^0} for $V_C(k)$ and $V_C(h)$, respectively, but they suggest as well that transitions through intermediate metastable states $V_C^-(k, C)$ and $V_C^-(h, D)$ have small capture barriers. From those configurations, a final conversion to ground state structures is only limited by very small transformation barriers. Hence, although it is reasonable to assume mechanisms involving direct transitions between ground states,

$$Z_1(-/0){:}V_C^0(h, B) + e^- \xrightarrow{\Delta E_\sigma \sim 0} V_C^-(h, C),$$

$$Z_2(-/0){:}V_C^0(k, B) + e^- \xrightarrow{\Delta E_\sigma \sim 0} V_C^-(k, D),$$

we actually cannot rule out the involvement of metastable states.

Regarding the capture of a second electron, we find that Z_1^- and Z_2^- behave differently, with the former essentially showing a vanishing capture barrier, while for Z_2^-, we could obtain a small but measurable barrier of $\Delta E_\sigma = 0.03$ eV. The calculations also anticipate a different mechanism for the second capture by the vacancy at the k- and h-sites. While in Fig. 9(a), the capture by $V_C^-(k)$ involving ground state structures $Q_{D^=/D^-}$ (blue lines) shows a very small capture barrier, the analogous transition involving ground state structures for $V_C^-(h)$ is shown in the middle inset of Fig. 9(a) and clearly results in a large barrier. Alternatively, we suggest that the transition takes place, firstly, via electron capture coupled to $Q_{C^=/C^-}$, which shows a minute barrier (right inset of Fig. 9), quickly followed the transformation toward the ground state $V_C^=(h, D)$ over a barrier which was calculated to be as low as 0.04 eV (see the left side of Fig. 1). Hence, for the second capture, we find

$$Z_1(=/-){:}V_C^-(h, C) + e^- \xrightarrow{\Delta E_\sigma \sim 0} V_C^=(h, C) \rightarrow V_C^=(h, D),$$

$$Z_2(=/-){:}V_C^-(k, D) + e^- \xrightarrow{\Delta E_\sigma = 0.03} V_C^=(k, D).$$

To conclude, we presented a joint experimental and theoretical investigation of the electronic properties of $Z_{1/2}$ traps in 4*H*-SiC. The study addressed the location of individual (−/0) and (=/−) transitions in the bandgap, as well as the capture and emission dynamics involving these traps. The experiments were carried out by conventional and high-resolution L-DLTS, whereas the calculations employed a plane-wave based density functional theory method using a semi-local approximation to the exchange-correlation energy.

We were able to confirm the connection between the levels of Z_1 and Z_2 with those of the carbon vacancy at the hexagonal and pseudo-cubic sites of the lattice, respectively. We also report direct capture cross section measurements for the levels. These show minute (or vanishing) capture barriers, confirming the calculated strong coupling between initial and final states involved in the transitions. Based on the calculated capture and transformation barriers, detailed mechanisms were proposed for the first and second electron capture.

ACKNOWLEDGMENTS

This work is supported by the NATO SPS programme (Project No. 985215). J.C. thanks the Fundação para a Ciência e a Tecnologia (FCT) for support under Project No. UID/CTM/50025/2013, co-funded by FEDER funds through the COMPETE 2020 Program. I.C. acknowledges financial support from the European Union through the Regional Development Fund for the "Center of Excellence for Advanced Materials and Sensing Devices" (Grant No. KK.01.1.1.01.0001), the European Union's Horizon 2020 Research and Innovation Programme under grant agreement No. 669014, and the European Union through the European Regional Development Fund - the Competitiveness and Cohesion Operational Programme (Grant No. KK.01.1.1.06). The work in Manchester has been funded by the UK EPSRC under Contract No. EP/P015581/1.

[1]T. Kimoto, Jpn. J. Appl. Phys. **54**, 040103 (2015).
[2]X. She, A. Q. Huang, O. Lucia, and B. Ozpineci, IEEE Trans. Ind. Electron. **64**, 8193 (2017).
[3]F. H. Ruddy, R. W. Flammang, and J. G. Seidel, Nucl. Instrum. Methods Phys. Res. A **598**, 518 (2009).
[4]T. R. Garcia, A. Kumar, B. Reinke, T. E. Blue, and W. Windl, Appl. Phys. Lett. **103**, 152108 (2013).
[5]J. Wu, Y. Jiang, M. Li, L. Zeng, J. Li, H. Gao, D. Zou, Z. Bai, C. Ye, W. Liang, S. Dai, Y. Lu, R. Rong, J. Du, and X. Fan, Rev. Sci. Instrum. **88**, 083301 (2017).
[6]*Silicon Carbide: Recent Major Advances*, Advanced Texts in Physics, edited by W. J. Choyke, H. Matsunami, and G. Pensl (Springer-Verlag, Berlin, 2004).
[7]V. Nagesh, J. W. Farmer, R. F. Davis, and H. S. Kong, Appl. Phys. Lett. **50**, 1138 (1987).
[8]L. Storasta, J. P. Bergman, E. Janzén, A. Henry, and J. Lu, J. Appl. Phys. **96**, 4909 (2004).
[9]T. Kimoto, A. Itoh, H. Matsunami, S. Sridhara, L. L. Clemen, R. P. Devaty, W. J. Choyke, T. Dalibor, C. Peppermüller, and G. Pensl, Appl. Phys. Lett. **67**, 2833 (1995).
[10]C. Hemmingsson, N. T. Son, O. Kordina, J. P. Bergman, E. Janzén, J. L. Lindström, S. Savage, and N. Nordell, J. Appl. Phys. **81**, 6155 (1997).
[11]G. Alfieri, E. V. Monakhov, B. G. Svensson, and M. K. Linnarsson, J. Appl. Phys. **98**, 043518 (2005).
[12]H. M. Ayedh, R. Nipoti, A. Hallén, and B. G. Svensson, Appl. Phys. Lett. **107**, 252102 (2015).
[13]M. E. Bathen, H. M. Ayedh, L. Vines, I. Farkas, E. Janzén, and B. G. Svensson, *Silicon Carbide and Related Materials 2017*, Materials Science Forum Vol. 924 (Trans Tech Publications, 2018), pp. 200–203.
[14]C. G. Hemmingsson, N. T. Son, A. Ellison, J. Zhang, and E. Janzén, Phys. Rev. B **58**, R10119 (1998).
[15]C. G. Hemmingsson, N. T. Son, A. Ellison, J. Zhang, and E. Janzén, Phys. Rev. B **59**, 7768 (1999).
[16]N. T. Son, X. T. Trinh, L. S. Løvlie, B. G. Svensson, K. Kawahara, J. Suda, T. Kimoto, T. Umeda, J. Isoya, T. Makino, T. Ohshima, and E. Janzén, Phys. Rev. Lett. **109**, 187603 (2012).
[17]H. M. Ayedh, V. Bobal, R. Nipoti, A. Hallén, and B. G. Svensson, J. Appl. Phys. **115**, 012005 (2014).
[18]G. D. Watkins, "Negative-*U* properties for defects in solids," in *Festkörperprobleme 24* (Springer-Verlag, Berlin, 1984), pp. 163–189.
[19]V. P. Markevich, L. I. Murin, T. Sekiguchi, and M. Suezawa, Mater. Sci. Forum **258–263**, 217 (1997).
[20]A. R. Peaker, V. P. Markevich, and J. Coutinho, J. Appl. Phys. **123**, 161559 (2018).
[21]D. V. Lang, J. Appl. Phys. **45**, 3023 (1974).
[22]L. Dobaczewski, A. R. Peaker, and K. B. Nielsen, J. Appl. Phys. **96**, 4689 (2004).
[23]I. Capan, T. Brodar, Ž. Pastuović, R. Siegele, T. Ohshima, S. ichiro Sato, T. Makino, L. Snoj, V. Radulović, J. Coutinho, V. J. B. Torres, and K. Demmouche, J. Appl. Phys. **123**, 161597 (2018).
[24]G. Alfieri and T. Kimoto, Appl. Phys. Lett. **102**, 152108 (2013).
[25]A. Koizumi, V. P. Markevich, N. Iwamoto, S. Sasaki, T. Ohshima, K. Kojima, T. Kimoto, K. Uchida, S. Nozaki, B. Hamilton, and A. R. Peaker, Appl. Phys. Lett. **102**, 032104 (2013).
[26]M. O. Aboelfotoh and J. P. Doyle, Phys. Rev. B **59**, 10823 (1999).
[27]A. Zywietz, J. Furthmüller, and F. Bechstedt, Phys. Rev. B **59**, 15166 (1999).
[28]L. Torpo, M. Marlo, T. E. M. Staab, and R. M. Nieminen, J. Phys. Condens. Matter **13**, 6203 (2001).
[29]M. Bockstedte, A. Marini, O. Pankratov, and A. Rubio, Phys. Rev. Lett. **105**, 026401 (2010).
[30]X. T. Trinh, K. Szász, T. Hornos, K. Kawahara, J. Suda, T. Kimoto, A. Gali, E. Janzén, and N. T. Son, Phys. Rev. B **88**, 235209 (2013).
[31]T. Hornos, A. Gali, and B. G. Svensson, Mater. Sci. Forum **679–680**, 261 (2011).
[32]J. Coutinho, V. J. B. Torres, K. Demmouche, and S. Öberg, Phys. Rev. B **96**, 174105 (2017).
[33]A. Alkauskas, Q. Yan, and C. G. V. de Walle, Phys. Rev. B **90** (2014).
[34]M. Ito, L. Storasta, and H. Tsuchida, Appl. Phys. Express **1**, 015001 (2008).
[35]G. Kresse and J. Hafner, Phys. Rev. B **47**, 558 (1993).
[36]G. Kresse and J. Hafner, Phys. Rev. B **49**, 14251 (1994).
[37]G. Kresse and J. Furthmüller, Phys. Rev. B **54**, 11169 (1996).
[38]P. E. Blöchl, Phys. Rev. B **50**, 17953 (1994).
[39]J. P. Perdew, K. Burke, and M. Ernzerhof, Phys. Rev. Lett. **77**, 3865 (1996).
[40]H. J. Monkhorst and J. D. Pack, Phys. Rev. B **13**, 5188 (1976).
[41]K. Huang and A. Rhys, Proc. R. Soc. A Math. Phys. Eng. Sci. **204**, 406 (1950).
[42]R. Kubo and Y. Toyozawa, Prog. Theor. Phys. **13**, 160 (1955).
[43]C. H. Henry and D. V. Lang, Phys. Rev. B **15**, 989 (1977).
[44]W. Shockley and W. T. Read, Phys. Rev. **87**, 835 (1952).
[45]R. N. Hall, Phys. Rev. **87**, 387 (1952).
[46]L. Shi and L.-W. Wang, Phys. Rev. Lett. **109**, 245501 (2012).
[47]A. M. Stoneham, Rep. Prog. Phys. **44**, 1251 (1981).
[48]S. Makram-Ebeid and M. Lannoo, Phys. Rev. B **25**, 6406 (1982).
[49]F. Schanovsky, W. Gös, and T. Grasser, J. Vac. Sci. Technol. B **29**, 01A201 (2011).